Limnol. Oceanogr., 59(5), 2014, 1637–1650

doi:10.4319/lo.2014.59.5.1637

Physical controls of oxygen fluxes at pelagic and benthic oxyclines in a lake

Julika Kreling,[1,*] Jenny Bravidor,[2] Daniel F. McGinnis,[3,4,a] Matthias Koschorreck,[2] and Andreas Lorke [1]

[1] University of Koblenz–Landau, Institute for Environmental Sciences, Landau, Germany
[2] UFZ—Helmholtz Centre for Environmental Research, Department Lake Research, Magdeburg, Germany
[3] University of Southern Denmark, Nordic Center for Earth Evolution (NordCEE), Institute of Biology, Odense, Denmark
[4] Helmholtz Centre for Ocean Research Kiel (GEOMAR), Kiel, Germany

Abstract

We compared oxygen fluxes measured simultaneously at the pelagic and benthic oxycline in a lake and analyze their relation to hydrodynamic forcing conditions. While the mean oxygen fluxes did not differ significantly among both sites, the fluxes were highly variable in time. Short energetic periods contributed disproportionately to the overall oxygen flux above both the benthic and pelagic oxycline. In the pelagic region, mean fluxes across the oxycline were limited by low diffusivities (7×10^{-8} m^2 s^{-1}) and were one to two orders of magnitude smaller than fluxes above the oxycline (0.5 and 32 mmol m^{-2} d^{-1}, respectively). A one-dimensional transport model was used to estimate sources and sinks of oxygen potentially causing this imbalance. The model results indicate that 92% of dissolved oxygen transported into the oxycline is used by the respiration of organic material imported into the oxycline from the epilimnion; chemical oxygen consumption associated with the upward flux of reduced substances is negligible. Our findings indicate that under such conditions, dissolved oxygen consumption and therewith mineralization within the oxycline can be comparable with the corresponding rates occurring in the sediments of eutrophic lakes with an oxic hypolimnion.

Anoxic conditions prevail in bottom waters of many stratified water bodies like lakes, reservoirs, and oceans. These conditions arise from an imbalance in the biogeochemical uptake and downward vertical transport of dissolved oxygen (DO), which can result from eutrophication (Wetzel 2001) and/or limited vertical mixing (Boehrer and Schultze 2008). While the former enhances the input of organic matter to the bottom waters and leads to an increased DO demand, the latter restricts downward fluxes and oxygen replenishment. Deep-water DO can be depleted either temporarily, during the seasonal cycle of density stratification (Turner and Erskine 2005), or permanently if meromixis inhibits seasonal mixing (Rodrigo et al. 2001). The so-called oxycline forms at the boundary between oxic surface waters and anoxic bottom waters. We define the oxycline as the layer ranging from the depth where the DO is 62.5 μmol L^{-1} to the depth where the DO becomes 0 μmol L^{-1}; it is congruent with the hypoxic zone. Pelagic oxyclines exhibit strong vertical gradients not only in dissolved substances, but also in biodiversity and ecosystem functioning. The lack of DO results in drastic habitat alterations (Zhang et al. 2009) and affects chemical cycling (Davison 1981). Inland water bodies are likely to be more susceptible to anoxia more frequently in the future since climate warming leads to longer stratification periods and thereby promotes the additional formation and persistence of anoxic conditions (Adrian et al. 1995; Livingstone 2003; Foley et al. 2012). Therefore, a process-based understanding of vertical oxygen transport between the oxic surface water and anoxic bottom layers becomes increasingly important. From a physical point of view, the transport across the oxycline is a function of turbulent diffusivity K_z and the prevailing concentration gradient $\partial C/\partial z$, and under turbulent flow conditions it can be assessed as the mean correlation of the turbulent fluctuations of concentration (C') and of vertical velocity (w'):

$$F = -K_z \cdot \partial C/\partial z = \overline{w' \cdot C'} \quad (1)$$

where the overbar denotes temporal averaging.

Turbulent transport is energized by wind, internal waves, or buoyancy-driven currents (Imberger 1998; Wüest and Lorke 2003) and thus is highly variable in space and time. This high temporal variability of the resulting DO fluxes has been studied intensively in the benthic zone (Lorke et al. 2003; Brand et al. 2008; Bryant et al. 2010). However, in the pelagic zone, only an indirect assessment exists where Bouffard et al. (2013) recently demonstrated the potential effect of highly variable physical forcing on vertical DO fluxes by inferring temporal variations of turbulent transport from time series of current shear and density stratification. Here, we apply the eddy correlation (EC) technique to quantify the high-frequency temporal variability of DO fluxes within the water column and above the sediment–water interface in a lake. The flux observations are complemented by detailed measurements of current velocity, density stratification, and concentrations of DO and other redox-relevant dissolved substances.

The objectives of this study are to compare the magnitude and variability of turbulent DO fluxes above the pelagic and benthic oxyclines of a stratified lake and to relate the observed flux variability to the hydrodynamic

* Corresponding author: kreling@uni-landau.de

[a] Present address: Leibniz-Institute of Freshwater Ecology and Inland Fisheries (IGB), Experimental Limnology, Berlin, Germany

forcing at both sites. The data are used to present a process-based approach to investigate DO exchange across oxyclines, where we analyze stratification and hydrodynamic regimes, including turbulence and vertical transport and we combine the fluxes with observed changes in bulk parameters to develop a one-dimensional mass balance covering the epilimnion and the oxycline. We conclude with discussing our findings in the context of the relevance of pelagic oxyclines for lake-internal nutrient and carbon cycling.

Methods

Measurements—Field site: Lake Scharmützelsee is located 50 km southeast of Berlin, Germany (52.25°N, 14.05°E; Fig. 1). It is of glacial origin and has an elongated shape (1.5 km wide and 10 km long) with a mean depth of 8.9 m and a maximum depth of 29.5 m. A more detailed description of the lake is provided by Grüneberg et al. (2011). The dimictic lake develops an anoxic hypolimnion during summer stratification (Kleeberg 1997). During a field campaign from 06 to 11 August 2012 we measured vertical fluxes of DO above the oxycline in the pelagic zone (Sta. P) as well as at the sediment–water interface near the southern shore at a depth of 6.1 m (Sta. S). The EC flux measurements were complemented by continuous (moored) observations of current velocity, thermal stratification, and DO across the oxycline, as well as by frequent vertical profiling of temperature, DO, and temperature microstructure throughout the entire water column at both stations. Additionally, water samples from the pelagic zone were analyzed for reduced substances (Fig. 2A).

Eddy correlation technique: The EC technique enables a direct, noninvasive, and quasi-continuous measurement of oxygen fluxes by recording fluctuations of DO concentration and vertical current velocity simultaneously (Eq. 1). Data processing preceding the final flux calculation typically includes despiking of sensor signals, rotation of coordinates, calculation of fluctuation components, and correction of timeshift (McGinnis et al. 2008; Lorrai et al. 2010; Lorke et al. 2013). The application within the water column requires a flux calculation from a limited frequency range of the cospectrum to exclude mooring motions and wave contributions.

EC systems were deployed during the field campaign at Stas. P and S. The pelagic system (henceforth referred to as EC_P) was deployed above the oxycline in 3.3 to 3.7 m depth. The instrument was mounted on a tensioned mooring line attached to a subsurface float at ~ 1 m depth and a loose tether to a surface float to minimize wave- and wind-induced motions (data were corrected for residual mooring motions, *see* data analysis). EC_P consisted of an acoustic Doppler velocimeter (ADV, Nortek Vector), which recorded current velocity and direction in a 1.5 cm high and 1 cm wide sampling volume at a sampling frequency of 8 Hz. A Clark-type microelectrode (ME) for DO measurements (Revsbech 1989) was attached to a custom picoamplifier (*see* McGinnis et al. 2011 for complete description) and connected to the ADV via its analog input port. The sensor was positioned within 1 cm

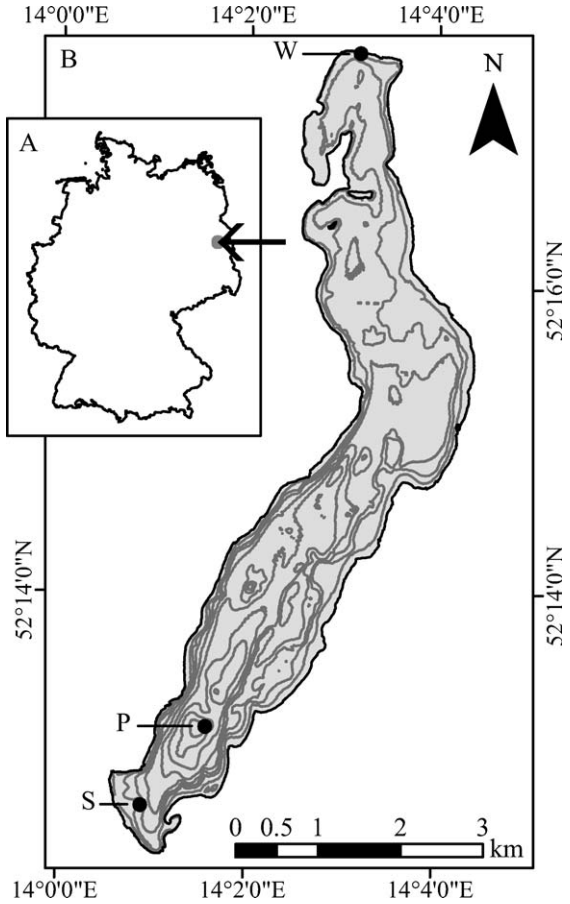

Fig. 1. (A) Location of Lake Scharmützelsee within Germany (arrow). (B) Bathymetric map of Lake Scharmützelsee with 4 m depth contours from 2 to 30 m depth. The locations of Sta. P and Sta. S, and weather station W are indicated.

distance to the ADV sampling volume. Additionally, EC_P was equipped with three optical sensors for DO (micro-optodes, OXR50 and OXR50-HS, PyroScience) with a separate logging unit. The high-speed micro-optode (MO) with a 90% nominal response time of < 0.8 s was positioned near ME and sampled at 6 Hz. The two other micro-optodes sampled at 0.40 m above and 0.29 m below the ADV sampling volume with a 1 min resolution. Temperature was measured at the depths of the micro-optodes using three thermistors (TR-1060 and TDR-2050, RBR) with a sampling frequency of 1 Hz; one of these sensors additionally measured pressure. All instruments were mounted on a metal frame (Fig. 2B). EC_P was deployed two times during the field campaign, from 06 August 2012 at 20:15 h to 08 August 2012 at 03:40 h at 3.7 m depth and from 08 August 2012 at 11:55 h to 15:18 h at 3.3 m depth for 31.4 h and 3.4 h of observation, respectively.

The second eddy correlation system (EC_S) was deployed above the sediment surface using a benthic lander at Sta. S (6.3 m depth). The instrumentation was identical to EC_P except for the following differences: Two analog input ports were equipped with oxygen microelectrodes, and the EC sampling volume was located 0.23 m above the

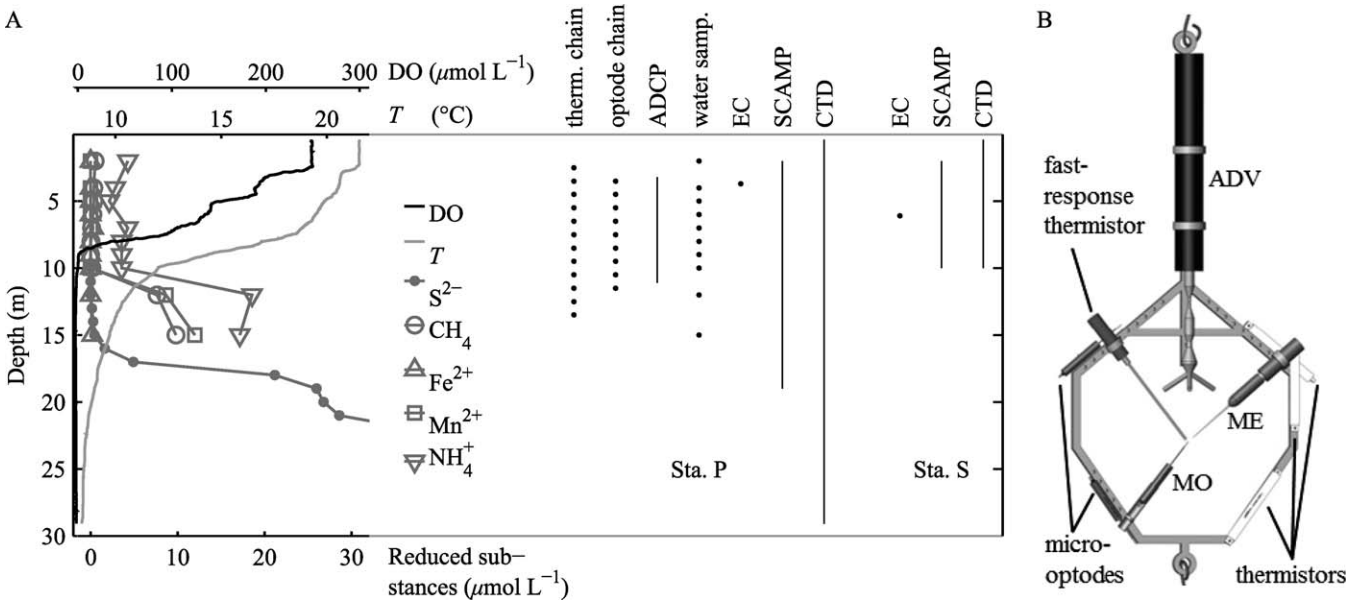

Fig. 2. (A) Depth profiles of DO, temperature (T), and concentration of reduced substances measured at Sta. P (left) on 07 August 2012 at 14:35 h, (middle) together with sampling depth of all measurements conducted at Sta. P (therm. = thermistor and samp. = samples) and (right) Sta. S. (B) Mounting of EC_P on an in-line metal frame for moored eddy correlation applications.

sediment surface. Micro-optodes and thermistors were positioned 0.39 m above and 0.14 m below the sampling volume, and the ADV recorded at 64 Hz (all data were averaged to 8 Hz for analysis). The deployment lasted from 07 August 2012 at 15:45 h to 09 August 2012 at 10:43 h for 43 h, but all micro-optodes stopped logging after 20.2 h of measurements.

Postprocessing of EC data included filtering of ADV data to remove bad quality data. Data with a beam correlation $< 70\%$ and a signal-to-noise < 12 dB were discarded. Additionally, all three velocity components were despiked using the phase–space method (Goring and Nikora 2002). Raw data recorded by the micro-optodes were converted to DO concentrations by means of technical equations provided by the manufacturer using the actual temperature measurements from the corresponding thermistors. Clock offsets between the ADV and optode logging unit were corrected by finding the maximum cross-covariance between microelectrode and micro-optode signal and shifting optode data in time accordingly. The same procedure was applied to remove a potential time offset between the thermistors and ADV. Calibration of analog input signals was accomplished by applying a linear regression to all readings of the microelectrode vs. the corresponding micro-optode.

ADCP: An acoustic Doppler current profiler (ADCP, Workhorse Sentinel 600 kHz; RD Instruments) was deployed for the entire field campaign at 11.4 m depth at Sta. P. The instrument was mounted upward looking on a mooring and measured vertical profiles of the three-dimensional current velocity between 3.2 and 11.1 m depth with a vertical resolution (bin size) of 0.1 m (Fig. 2A). Averages of three individual velocity measurements were recorded every 3 s. The instrument was operated in pulse coherent mode (RDI mode 5) providing a nominal standard deviation of 0.35 cm s^{-1}.

Thermistor and optode chain: Twelve temperature loggers (TR-1060 and TR-1050 with 3 s response time, RBR) were moored at Sta. P between 2.5 and 13.5 m depth with a vertical spacing of 1 m. Temperature was measured every second with an accuracy of $\pm$ 0.002°C. Also at Sta. P, DO concentration was measured between 3.5 and 11.5 m depth with a sampling interval of 1 min using nine optical sensors (D-Opto-Logger, Zebra-Tech; Rinko ARO-USB, JFE Advantech and miniDOT, Precision Measurement Engineering). All sensors were calibrated before the deployment except for the miniDOT. Thermistor, optode, and ADCP measurements, respectively, are illustrated in Fig. 2A.

Turbulence profiling: For quantifying turbulence intensity and transport, temperature microstructure profiles were measured using a self-contained autonomous microstructure profiler (SCAMP; Precision Measurement Engineering). SCAMP contained two fast-response thermistors (FP07), which sampled at a frequency of 100 Hz while the probe sank freely through the water column at ~ 0.12 m s^{-1}. Measurements were conducted at both stations during the time of maximum cooling at the water surface (around sunrise on 08, 09, and 10 August 2012), and during the time of maximum heating (in the afternoon on 07, 08, 09, and 10 August 2012). For each sampling, a set of nine profiles was collected with approximately 8 min between individual profiles. Profiles at Sta. S were measured approximately 60 m southeast of EC_S at about 10 m depth and covered the whole water column. Profiles at Sta. P reached from the surface down to 19 m depth (Fig. 2A).

CTD: Depth profiles of temperature and DO were measured at Stas. P and S using a conductivity–temperature–depth (CTD) probe (CTD48M, Sea & Sun Technol-

ogy; with a fast DO sensor, AMT Analysenmesstechnik). Whole water-column profiling was performed whenever a set of microstructure profiles was measured (*see* above) and additionally around sunrise on 07 August 2012.

Water samples: Water samples were collected at Sta. P in the afternoon on 07 and 09 August and around sunrise on 08 and 10 August 2012 at 2, 4, 5, 6, 7, 8, 9, 10, 12, and 15 m depth (Fig. 2A) and were analyzed for the following reduced substances: dissolved iron (Fe^{2+}), dissolved manganese (Mn^{2+}), ammonium (NH_4^+), and dissolved methane (CH_4). Samples for chemical analyses of Fe^{2+} and Mn^{2+} (filtered with 0.45 μm Satorius Minisart filters) were acidified with HNO_3, stored in polyethylene bottles, and analyzed using inductively coupled plasma optical emission spectrometry (Perkin Elmer). Analysis of NH_4^+ was performed photometrically according to standard 38406-E5 of the German Institute for Standardization (Deutsches Institut für Normung), and analysis of CH_4 was performed according to Goldenfum (2010). Total sulfide (S^{2-}) concentrations were analyzed following Kleeberg (1997) for an additional set of water samples collected at Sta. P on 07 August 2012 between 10 and 29 m depth with 1 m resolution.

Weather: The average wind speed and wind direction over 10 min was obtained from a weather station operated by the Brandenburg University of Technology Cottbus-Senftenberg at the northern tip of the lake (Fig. 1B).

Data analysis—EC oxygen fluxes: Measured EC data were used to calculate turbulent DO fluxes using microelectrode and micro-optode measurements at the depth of the respective deployments. Measured data were divided in 1024 s (8192 samples) long segments with a 50% overlap resulting in flux estimates with a temporal resolution of 8.5 min. All following steps were conducted for each of these segments. Three-dimensional current velocities measured by the ADV were double-rotated into the direction of mean flow velocity for EC_P. For EC_S double rotation was not applicable as a result of oscillating flow directions, and a planar fit rotation was applied to the entire dataset (Lorke et al. 2013). Microelectrode and micro-optode measurements (summarized as concentration C) and the vertical component of the rotated current velocity w were linearly detrended to derive the fluctuation components C' and w' (Moncrieff et al. 2010).

A time shift was applied to each segment of EC_P and EC_S to compensate for the travel time resulting from the slight horizontal displacements between the sampling locations of the ADV and sensors. The recorded time series of C' and w' were shifted relative to each other within each segment to reach the maximum cross-correlation, which generally corresponds to the maximum flux (McGinnis et al. 2008; Lorrai et al. 2010).

Occurrence of internal waves and surface waves precluded the usual method of calculating fluxes via a multiplication of C' and w' followed by temporal averaging. Instead the co-spectral density of C' and w' was calculated using Welch's method (Emery and Thomson 1997). Fluxes were calculated by integrating the spectra from frequencies of 1/3 Hz to 1/30 Hz. This procedure excludes co-spectral variance at higher and lower frequencies, which is associated with surface and internal waves, respectively (*see* Results). Therefore, obtained fluxes are likely to present lower bounds of actual fluxes by neglecting flux contributions at frequencies masked by waves.

Further deployments of the eddy mounting used for EC_P at greater depth, where surface waves are unlikely to occur, indicate that vibrations of the mooring cause a distinct peak in the frequency spectra of vertical velocity at a frequency of 1.36 Hz (J. Kreling unpubl. data). Therefore, it can be assumed that vibrations and high-frequency oscillations of the mooring contribute to the variance at frequencies $>$ 1/3 Hz in addition to surface waves in the presented dataset. Nevertheless, the described way of processing excludes both mooring vibration and surface wave contributions from flux calculations.

Dissipation rates of turbulent kinetic energy: Dissipation rates of turbulent kinetic energy (ε) were estimated from the ADV velocity measurements using the inertial dissipation method (Lorke and Wüest 2005). Therefore, we calculated wave number spectra from the fluctuations in the rotated longitudinal velocity component for each 1024 s long segment and fitted the Kolmogorov slope $k^{-5/3}$ (k denotes wave number) to the inertial subrange of these spectra. As analyzed by Bluteau et al. (2011), the longitudinal velocity component is least affected by anisotropy of turbulence in density-stratified environments. The wave number range used for spectral fitting under the assumption of Taylor's hypothesis corresponded to the frequency limits of the flux calculation. Spectral fitting was performed using the maximum-likelihood method described in Bluteau et al. (2011). As a measure of variance of the log-normally distributed dissipation rates, the intermittency factor was calculated according to Baker and Gibson (1987).

Turbulence profiling: Dissipation rates of turbulent kinetic energy (ε) and turbulent diffusivity (K_z) were derived from temperature microstructure profiles: We calculated ε for vertical segments of 0.2 m by fitting the temperature gradient spectrum from microstructure profiles to the theoretical Batchelor spectrum following the maximum-likelihood method of Ruddick et al. (2000) and the methods of Steinbuck et al. (2009). Fits with a signal-to-noise ratio $>$ 1.3, a logarithm of the likelihood ratio $>$ 2, and a mean absolute deviation $> 2(2/d)^{1/2}$ with d (degrees of freedom) = 4 were considered for further analysis (Ruddick et al. 2000). Turbulent diffusivity (K_z) was estimated according to the parameterization of Shih et al. (2005) and the modifications of Bouffard and Boegman (2013) with Prandtl number = 700 and the energetic regime starting from turbulence intensity parameter = 400. For presentation purposes, results for the 0.2 m segments from individual profiles and both sensors were combined by calculating the logarithmic mean within 0.4 m depth segments. The log-mean was chosen because variability of K_z was mainly caused by variations of measured dissipation rates, which are log-normally distributed in homogenous turbulence (Davis 1996). DO fluxes at the depth of the oxycline (F) were calculated following Eq. 1 using log-mean diffusivities from microstructure profiles (K_z) and vertical DO gradients (dC/dz) from CTD profiles. To account for the analytical precision of in situ probe readings, we

considered sensor readings < 1.6 μmol L^{-1} as zero DO to define the lower bound of the oxycline.

Characterization of internal waves: As a measure of intensity of progressive high-frequency internal waves, we integrated the spectral variance of vertical velocity fluctuations measured by the ADV of EC_P and EC_S between frequencies of 1/1024 Hz and 1/30 Hz for each segment. In linear wave theory, this variance scales with the kinetic energy of orbital water motions.

The period of the basin-scale internal seiche (T) was estimated using the generalized two-layer Merian Formula

$$T_n = \frac{2L}{n} \cdot (g' h')^{-0.5} \quad (2)$$

for a mode 1 (n) wave with L denoting the length of the basin and $g' = (\Delta\rho/\rho) \cdot g$ and $h' = h_1 h_2/(h_1 + h_2)$ denoting reduced gravity and depth (with ρ = density of water, $\Delta\rho$ = density difference between layers, g = acceleration of gravity, and h_1 and h_2 = depth of layers; Imboden and Wüest 1995).

Gradient Richardson number: The gradient Richardson number (Ri) as a measure of the stability of stratified shear flow is calculated as the ratio of buoyancy frequency N^2 and current shear S^2:

$$Ri = N^2/S^2 \quad (3)$$

Buoyancy frequency ($N^2 = -g/\rho_0 \times \partial\rho/\partial z$, ρ denoting density and g gravitational acceleration) was calculated from thermistor chain measurements. Temperatures were averaged to the ADCP measurement intervals, interpolated linearly to the depth of the ADCP measurement (z) and converted to density (ρ) following Chen and Millero (1977) using zero salinity. Current shear ($S^2 = (\partial U/\partial z)^2$ with U denoting horizontal current speed) was estimated from ADCP measurements. The rather small extent of vertical averaging of N^2 and S^2 of 0.1 m was chosen to account for the strong vertical gradients of stratification and current shear within and above the oxycline. Calculating Ri over a vertical length scale of 0.5 or 1 m does not change the results considerably.

Results

Hydrodynamic conditions, DO, and temperature stratification—During the field campaign, the lake was thermally stratified with a mean temperature of 19–22°C in the epilimnion and 8.4–11°C in the hypolimnion. The thermocline, defined as the depth of maximal buoyancy frequency N^2, was located at $\sim$ 9 m depth in the first half of the measurement campaign and subsequently moved upward toward the end of the measurement period, while isotherms became wider spaced. Simultaneously, higher temperatures penetrated to greater depths (Fig. 3A). Oxygen concentrations in the epilimnion ranged from 94 to 297 μmol L^{-1}, and surface waters became occasionally oversaturated with oxygen up to 110% saturation. Decreasing oxygen concentrations were observed starting from 3 to 6 m depth, and hypolimnic waters became anoxic at $\sim$ 9–10 m depth. In the first half of the campaign, the hypoxic zone moved up and down, following the period of the basin wide internal seiche ($T \approx 20$ h), but became more stable and thinner during the second half of the campaign (Fig. 3B). The average wind speed was 2.0 ± 1.2 m s^{-1}, but wind varied diurnally with a maximum speed of 5.6 m s^{-1} in the afternoon of 07 August 2012 (Fig. 4A). Wind direction was slowly changing from southeast to northwest during the measurement period but with predominately eastward directed winds.

Observed currents at Sta. P were mainly directed along the longitudinal lake axis and were up to 0.15 m s^{-1} in magnitude (Fig. 3A). Considerable currents directed perpendicular to the longitudinal lake axis only occurred on 07 and 08 August above 4 to 5 m depth. ADCP data revealed the frequent occurrence of opposing currents separated at 4 to 5 m water depth. At Sta. EC_S maximum flow velocities were about two times smaller than at Sta. EC_P, and intermittent periods of very low flow velocities were observed (< 0.01 m s^{-1}, Fig. 4B). The flow was predominantly directed in the north–south direction. The strongest dynamics was observed in the afternoon of 07 August 2012, when a strong jet-like current at the depth of the thermocline had the highest observed current speeds and vertical displacement of isotherms and DO isolines with a maximum of 0.5 m. The displacement was caused by high-frequency internal waves, with periods of 5–7 min (Fig. 5). These propagating waves were present at Sta. P throughout the measurement period. Observed frequencies of internal waves were close to the maximum possible frequency supported by density stratification ($f_{max} = N/2\pi$). Internal wave intensity was about six times higher at EC_P (mean of whole dataset $8.1 \times 10^{-6} \pm 1.1 \times 10^{-5}$ m^2 s^{-2}) than at EC_S (mean $1.2 \times 10^{-6} \pm 1.2 \times 10^{-6}$ m^2 s^{-2}, Fig. 3F). At Sta. P a peak in wave intensity is visible in the morning of 07 August 2012, whereas wave intensity at Sta. S fluctuates with a period similar to the one of the basin wide internal seiche ($T \approx 20$ h). Furthermore surface waves or mooring vibrations (*see* Methods) with periods of 0.7–3 s were present at EC_P but not at EC_S.

Turbulence and transport—Dissipation rates of turbulent kinetic energy (ε) derived from temperature microstructure profiles at Sta. P were decreasing with depth from about 10^{-7} W kg^{-1} at 2 m to 10^{-9} W kg^{-1} at 19 m (Fig. 6B). Compared with Sta. P, ε at Sta. S was up to one order of magnitude smaller above 6 m depth and in the same range for greater depths. These differences between the two stations became less pronounced toward the end of the measurement period. Time series of ε obtained from the ADV ranged from 7.0×10^{-9} to 2.3×10^{-6} W kg^{-1} and differed significantly between the two sampling sites by a factor of 2 (mean of whole dataset, P, 1.7×10^{-7} W kg^{-1} with an intermittency factor of 0.44; S, 8.1×10^{-8} W kg^{-1} with an intermittency factor of 0.35). Sta. P revealed a high temporal variability (Fig. 3E), especially on 07 August 2012 at 07:00 h, when ε obtained from EC_P showed a sudden increase by nearly two orders of magnitude. Turbulence at EC_P and EC_S was strongly affected by density stratification, which is described by the turbulence intensity parameter I and is the ratio of Ozmidov and Kolmogorov

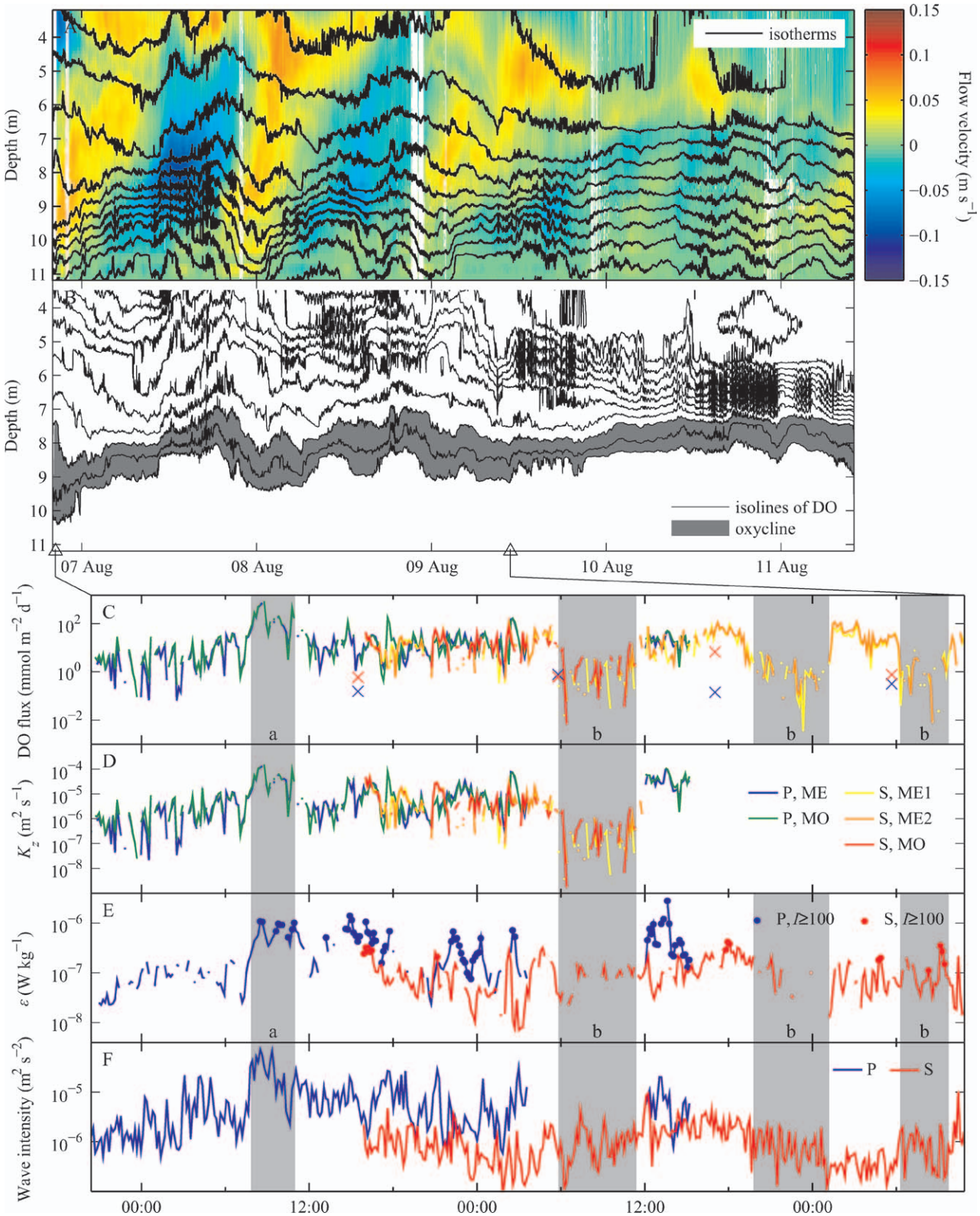

Fig. 3. (A) Horizontal flow velocity in direction of the longitudinal lake axis and isotherms (from bottom to top: 11°C to 21°C with 1°C increment). (B) Isolines of DO (from bottom to top: 12.5, 31.3, to 313 μmol L^{-1} with 31.3 μmol L^{-1} increment) with depth of oxycline indicated by gray color (here the lower bound is defined as the depth of 12.5 μmol DO L^{-1}). (C) Downward directed DO fluxes measured with microelectrode (ME) and micro-optode (MO) from EC_P and EC_S and DO flux across oxycline at Sta. P (x), and Sta. S (x). Shaded areas mark (a) the flux event and (b) periods of low flux discussed in the text. (D) Diffusivities (K_z) calculated from the fluxes shown in (C) and corresponding DO gradients. (E) Dissipation rates of turbulent kinetic energy (ε) at Sta. P and Sta. S derived from EC_P and EC_S. Dots mark dissipations rates with $I \geq 100$. (F) Internal wave intensity at Sta. P and Sta. S.

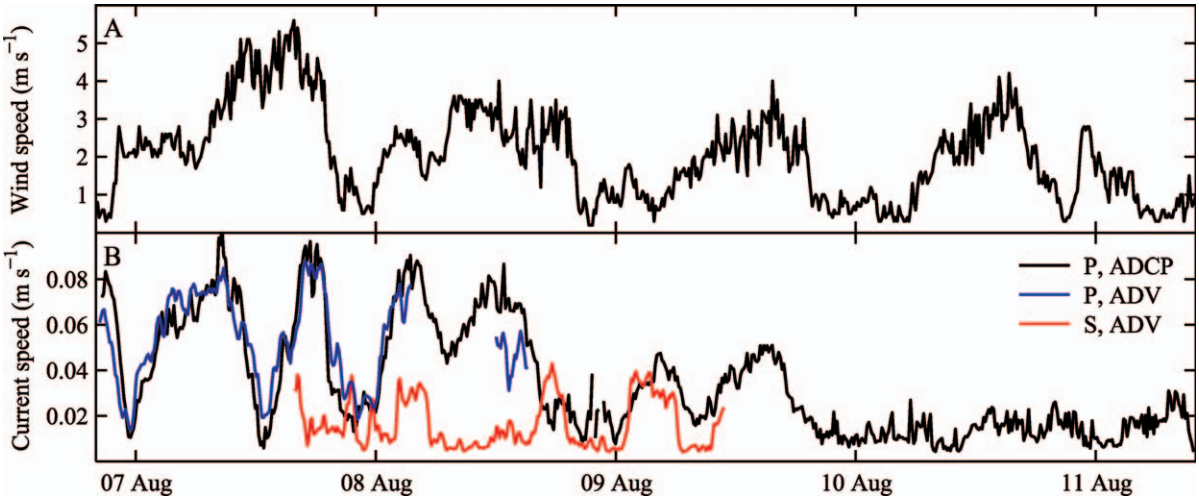

Fig. 4. (A) 10 min average of wind speed. (B) 10 min average of current speed measured by ADCP at Sta. P at the depth of EC_P deployment 1 and segment-mean (8.5 min) current speed measured by EC_P and EC_S.

length scales (here we use the modified form of $I = (\varepsilon/\nu N^2)^{3/4}$ following Gargett et al. (1984), with ν denoting kinematic viscosity of water). According to Gargett et al. (1984) the narrow inertial subrange in turbulence spectra with $I < 100$ does not allow for estimating dissipation rates from inertial subrange fitting. In our analysis we calculated ε for $I < 100$ as long as a reasonable fit of the inertial subrange to the spectra was found, being aware of that these data need careful interpretation and potentially have only limited explanatory power.

Depth profiles of turbulent diffusivity K_z (from microstructure profiles) revealed that high turbulent diffusivities up to 4×10^{-4} m^2 s^{-1} only occurred down to 4 m depth during the first half of the measurement period and deepened down to 6 m depth in the second half (Fig. 6C). At the depth of the oxycline, turbulent diffusivities were in the order of 10^{-8} to 10^{-7} m^2 s^{-1}, i.e., in the order of molecular diffusion of heat and lower (with the exception of the afternoon measurement on 08 August 2012 at Sta. S). Below these depths, vertical transport increased and varied predominantly in the range of 10^{-7} to 10^{-5} m^2 s^{-1}. The gradient Richardson number, which provides a measure of stability for stratified shear flows, indicates the absence of turbulent transport within and below the thermocline. Values greater than 0.25 indicate that stratification suppresses turbulence, and therefore vertical transport is restricted to molecular diffusion, while the flow might become unstable and turbulent mixing could prevail for $Ri < 0.25$ (Miles 1961). Gradient Richardson numbers smaller than the critical value were only observed in the epilimnion, whereas at the depth of the oxycline the flow was predominantly stable (Fig. 6A). Even the strong metalimnic jet occurring in the afternoon of 07 August 2012 at 7 to 9 m depth (Fig. 3C) could not entail turbulence at the depth of the oxycline.

Time series of turbulent diffusivities at the depth of EC measurements were calculated for each segment using Eq. 1 with fluxes (F) obtained from EC_P and EC_S and oxygen concentration gradients (dC/dz) derived from micro-optode measurements above and below the flux sampling volume. Diffusivities calculated from EC fluxes were in the same range of 1.7×10^{-9} to 1.5×10^{-4} m^2 s^{-1} at both stations (Fig. 3D) and did not differ significantly. At Sta. P, diffusivities steeply increased by more than two orders of magnitude on 07 August 2012 at 07:00 h according to increasing ε.

Fluxes—Mean fluxes of DO were directed downward at both stations. DO fluxes obtained from EC_P generally ranged from −163 to 9 mmol m^{-2} d^{-1} (mean −15.4 mmol m^{-2} d^{-1}, ME) for most of the time, but increased by up to 50 times the mean during a single flux event that coincided with increased values in K_z, ε, and wave intensity (Fig. 3C, shaded area a). The pronounced flux event was evident in all fluxes of EC_P and took place in the morning of 07 August 2012 (07:50 h to 11:00 h), when 56% of

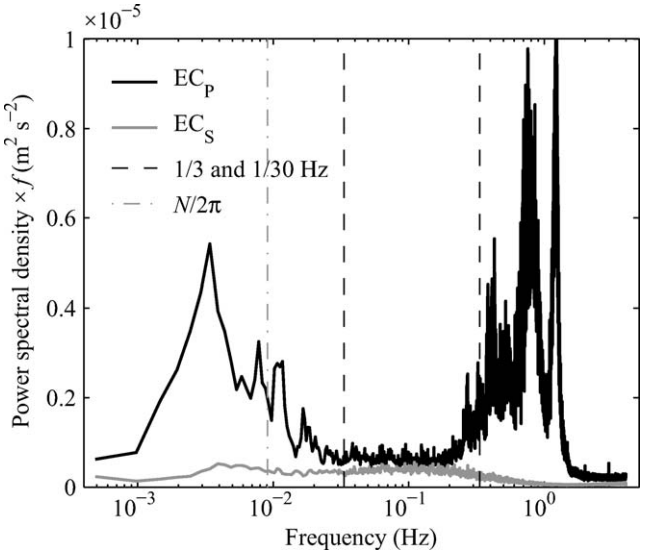

Fig. 5. Variance preserving power spectra of vertical velocity obtained from EC_S and EC_P (first deployment only). The black dotted vertical lines encompass the frequency range used for flux calculation, while the gray dash-dotted vertical line corresponds to the upper frequency limit for internal waves ($N/2\pi$) during the first deployment of EC_P.

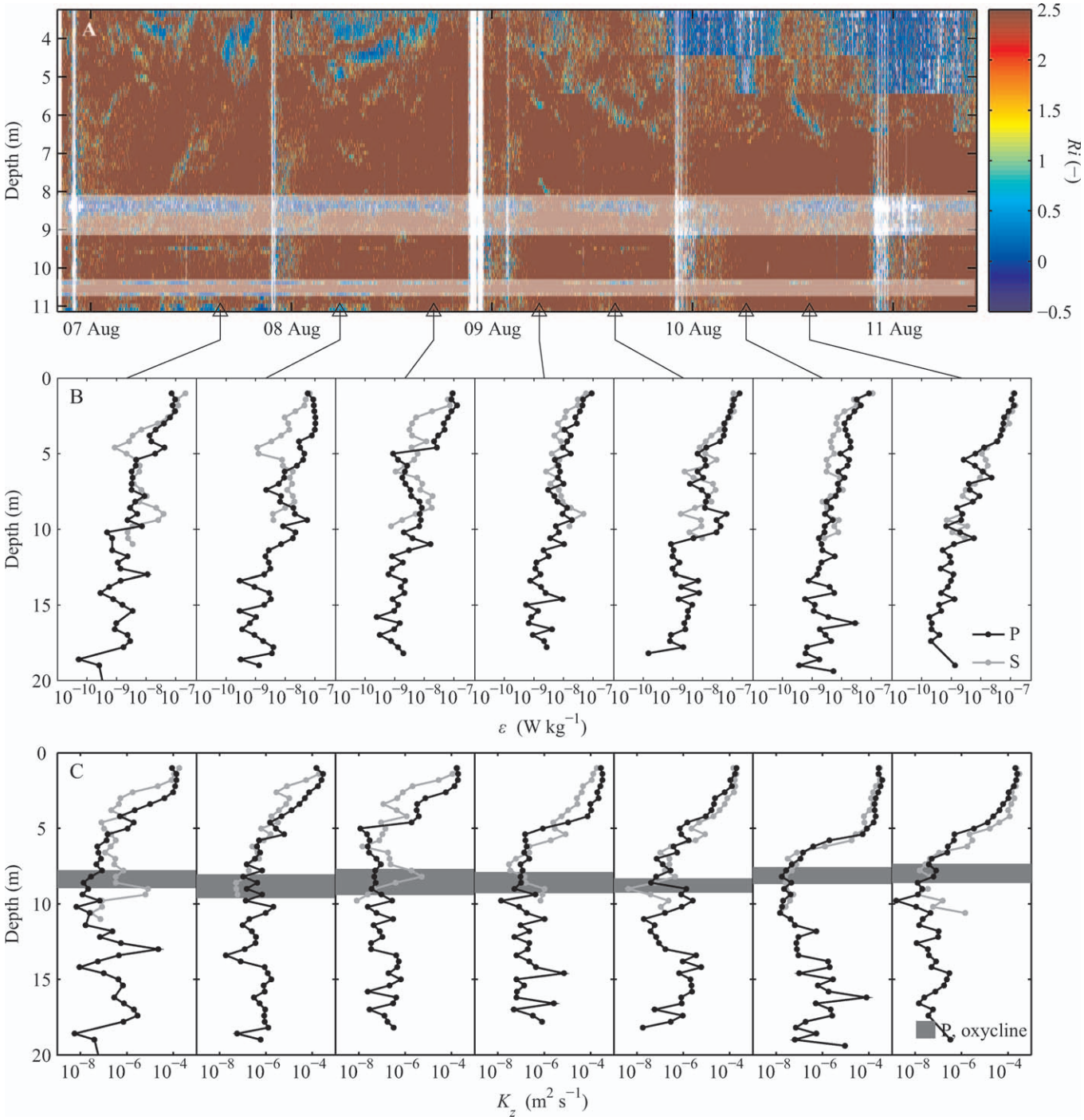

Fig. 6. (A) Gradient Richardson number *Ri* calculated from ADCP and thermistor data and averaged to 1 min time resolution (data covered by semitransparent bars had erroneous velocity measurements due to measurement interference with the water surface and were not considered in the analysis). (B) Depth profiles of average dissipation rates of turbulent kinetic energy (ε) and (C) average diffusivities (K_z) derived from microstructure profiles at Sta. P and Sta. S; gray bars denote the depth of the oxycline at Sta. P.

the total oxygen flux occurred in only a 3 h period, corresponding to 9.5% of the total measurement period. The mean DO flux obtained from EC_S was in the order of -10 mmol m^{-2} d^{-1} and comparable, i.e., not significantly different from the mean oxygen flux at EC_P (Fig. 3C; Table 1). However, the range of variability of DO fluxes at EC_S (-118 to 20 mmol m^{-2} d^{-1}, ME) was lower than at EC_P, even if the large flux event is excluded, but fluxes measured with EC_S still showed strong temporal variability (Fig. 3C). During three time periods covered by the microelectrode measurements at Sta. S, observed DO fluxes remained extremely low for several hours (08 August 05:50–11:23 h, 08 August 19:46–09 August 01:10 h, 09 August 06:17–09:43 h, Fig. 3C, shaded areas b). In total,

Table 1. Mean DO flux with standard deviation (SD), maximum (max), and minimum (min) in mmol m^{-2} d^{-1} measured with EC_P and EC_S using microelectrode (ME) and micro-optode (MO) in times excluding the flux event and minimum DO flux during flux event for EC_P.

		Excluding flux event			Including flux event	
	Sensor	Mean ± SD	Max	Min	Mean ± SD	Min
P	ME	−15.4±22.1	8.7	−163.3	−30.1±77.4	−711.0
	MO	−16.4±24.9	63.5	−177.1	−33.6±88.6	−844.4
S	ME1	−14.6±20.4	19.9	−110.3		
	ME2	−18.2±24.9	31.9	−118.0		
	MO	−10.7±14.5	28.8	−66.5		

these time periods contributed only 2% to the overall oxygen flux but represent one third of the total measurement time. Micro-optode measurements covered only the first of these periods, when 7% of total flux occurred in 27% of time. Mean fluxes and flux variability measured by micro-optodes at both sampling sites are summarized in Table 1. DO fluxes measured with micro-optode and microelectrode correlated well, showing correlation coefficients of 0.99 (Sta. P), 0.80, and 0.73 (Sta. S). Fluxes measured when EC_P and EC_S deployments were overlapping in time showed comparable characteristics.

In comparison with the observed fluxes at the depth of EC deployments, DO fluxes across the oxycline were one to two orders of magnitude smaller (Fig. 3C). Fluxes across the oxycline did not vary considerably with time, only the DO flux in the afternoon of 08 August at Sta. S was 13 times higher than the average observed flux across the oxycline at Sta. S.

Fluxes of all reduced substances were calculated according to Eq. 1 using log-mean diffusivity from microstructure profiles (K_z) and the concentration gradient ($\partial C/\partial z$) between 10 to 12 m depth. Measured concentrations were converted to their corresponding DO equivalent potentially consumed during oxidation and summed up to total DO equivalent flux (Matzinger et al. 2010; Müller et al. 2012). Resulting upward fluxes of reduced DO equivalents ranged from 34 to 363 μmol m^{-2} d^{-1} with a mean of 143 ± 155 μmol m^{-2} d^{-1}. On average CH_4 contributed most to the total DO equivalent flux (47.7%), followed by NH_4^+ (32%) and Mn^{2+} (20.4%). Measured Fe^{2+} and S^{2-} concentrations were below the detection limits of 0.01 and 0.1 mg L^{-1}, respectively, at the considered depths. As S^{2-} has a high detection limit (0.1 mg L^{-1}), we estimate the maximum possible contribution of S^{2-} to the total DO equivalent flux by assuming a maximum concentration difference of 0.1 mg L^{-1} within 10 to 12 m depth, which resulted in a mean total DO equivalent flux of 185 ± 211 μmol m^{-2} d^{-1} (including S^{2-}).

Discussion

Physical control of DO fluxes—We found that the vertical DO fluxes above and across the oxycline are controlled by different physical processes. Fluxes in the density-stratified water column above the oxycline are driven by turbulent diffusion, with diffusivities up to 10^5 times higher than molecular diffusion. A systematic dependence of the fluxes on oxygen gradients could not be observed (Fig. 7). Similar to the observations of Bouffard et al. (2013) in Lake Erie, flux magnitudes were highly

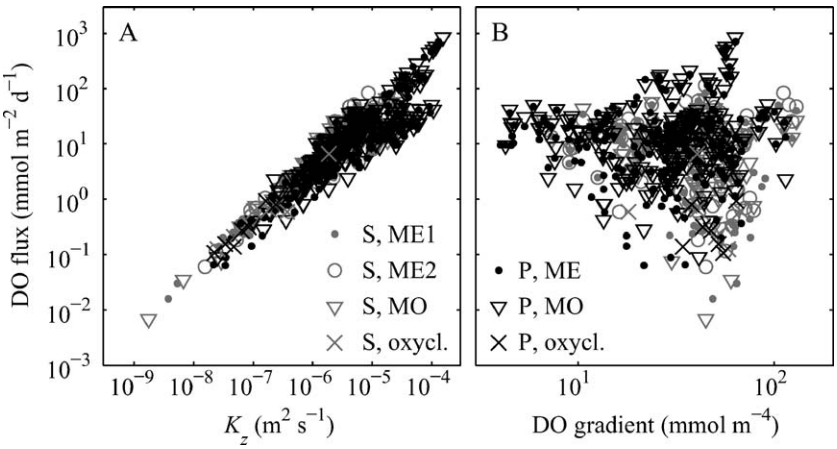

Fig. 7. (A) Magnitude of the downward directed DO flux across the oxycline (oxycl., derived from SCAMP profiles), and fluxes derived from microelectrode (ME), and micro-optode measurements (MO) at Sta. P and Sta. S as a function of diffusivity (K_z) and (B) as a function of the magnitude of the DO gradient.

variable in time, and short energetic periods contributed disproportionately to the overall DO flux above the benthic as well as above the pelagic oxycline. This temporal variability was caused by temporal variations of the turbulent diffusivity (Fig. 7). In stratified shear flows, turbulent vertical diffusivity K_z depends on the dissipation rate of turbulent kinetic energy ε, buoyancy frequency N^2, and the mixing efficiency γ_{mix}. The mixing efficiency is often assumed to be constant ($\gamma_{mix} = 0.2$; Wüest and Lorke 2003); however, its variability has been shown in laboratory experiments, numerical simulations, and in the field (Shih et al. 2005; Ivey et al. 2008; Dunckley et al. 2012). In our observations, time periods of high DO flux above the pelagic oxycline were characterized by increased rates of turbulent kinetic energy dissipation. Simultaneously, the intensity of progressive high-frequency internal waves was high during the flux events, and wave-induced shear can be considered as a major source of turbulence. Thus, the temporal variability of DO fluxes above the pelagic oxycline can be attributed to varying turbulent transport, which itself was influenced by the intensity of high-frequency internal waves. On the contrary, temporal variability in diffusivities above the benthic oxycline was related to the magnitude of flow velocity. In the boundary-layer flow above the sediment surface, flow velocity at a particular height is directly related to turbulent dissipation rates, which control vertical solute transport (Lorke et al. 2003). Therefore, temporal variability of pelagic and benthic oxygen fluxes were both governed by turbulent diffusivities, although the ultimate driving force for turbulence differed at these sites.

By considering a general measurement uncertainty of a factor of two (Kocsis et al. 1999; Lorke and Wüest 2005), dissipation rates of turbulent kinetic energy at the depth of EC measurements differed only insignificantly between the benthic and pelagic sampling sites. Additionally, microstructure profiles showed no pronounced differences in the distribution of turbulence with depth between these sites. Thus, our measurements revealed the same magnitude of turbulence in the benthic and pelagic region, which is contrary to observations in many other lakes of comparable size, showing enhanced mixing along the boundaries (Goudsmit et al. 1997). Enhanced boundary mixing is attributed to shoaling of high-frequency internal waves at the lake slopes (MacIntyre et al. 1999; Lorke 2007); however, these waves were only of minor intensity at the benthic sampling site, and enhanced turbulence due to shoaling could not be observed.

Although the oxycline was highly dynamic in terms of horizontal currents, vertical current shear, and depths of temperature and DO concentration isolines, turbulent mixing was attenuated by density stratification, and vertical fluxes are predominantly determined by low diffusion coefficients and strong vertical DO gradients. Nevertheless, a higher DO flux in the afternoon of 08 August (Sta. S) suggests that rare turbulent events in the oxycline can temporarily increase the flux by a factor of 13 (compared with the average flux). Although the statistics of these events is surely not resolved by our microstructure observations, this value is in close correspondence to Bouffard et al. (2013), who found 12 times higher fluxes from turbulent than from molecular diffusivities based on longer-term observations in Lake Erie.

A one-dimensional model of oxygen fluxes at the pelagic oxycline—Observed oxygen fluxes above the oxycline were up to two orders of magnitude higher than those across the oxycline. This flux imbalance either leads to temporal increase in DO concentration and progressive deepening of the oxycline or it is balanced by consumption of DO within the oxycline. In the following, we analyze the relative importance of oxygen consumption and transport using a one-dimensional model of DO dynamics at the oxycline.

Since observed DO and temperature dynamics were strongly affected by baroclinic motions caused by internal waves and wind-driven circulation (Fig. 3A,B), we estimate the DO mass balance at isothermal rather than at fixed depths. DO concentration C at an isothermal depth z^*, is governed by the divergence of the cross-isothermal (diapycnal) DO flux F_{DO} and the net volume-specific rate of oxygen consumption and production R_{net}:

$$\frac{\partial C(z^*,t)}{\partial t} = \frac{\partial}{\partial z^*}(F_{DO}) + R_{net} \tag{4}$$

R_{net} summarizes all DO sources and sinks at the corresponding isothermal depth and will be estimated in the following by quantifying all remaining terms of the mass balance in Eq. 4.

In our observations, the rate of change of DO concentration at isothermal depths (left-hand side of Eq. 4) was nearly constant over time and was affected neither by the observed variation of the DO flux nor by diurnal variations in DO production and consumption or heating (Fig. 8). While DO concentration is constantly increasing above the depth of the 20.5°C isotherm, it is equally decreasing at 17.5–19°C, where the 19°C isotherm approximately corresponds to the upper boundary of the oxycline. Therefore, temporal DO concentration change within the oxycline was derived by linear regression of DO concentrations vs. time at the depth of the 17.5°C isotherm (Fig. 8) and accounts for -6.6 μmol L^{-1} d^{-1}.

The flux divergence of DO within the oxycline (first term on the right-hand side of Eq. 4) can be estimated from Fick's law (Eq. 1). The corresponding diffusion coefficient can be considered to be $D_{DO} = 7 \times 10^{-8}$ m^2 s^{-1}, which is the log-mean diffusivity at the depth of the pelagic oxycline derived from microstructure measurements, resulting in

$$\frac{\partial}{\partial z^*}(F_{DO}) = \frac{\partial}{\partial z^*}\left(K_z \cdot \frac{\partial C}{\partial z^*}\right) \approx D_{DO} \cdot \frac{\partial^2 C}{\partial z^{*2}} \tag{5}$$

The second-order cross-isothermal derivative of DO has a maximum magnitude of ≈ -63 mmol m^{-5}. Thus, the term describing the effect of vertical mixing on temporal DO concentration changes at isothermal depths is -0.4 μmol L^{-1} d^{-1}. Therefore, DO transport is an order of magnitude smaller than observed temporal DO concentration changes within the oxycline (-6.6 μmol L^{-1} d^{-1}), accounting for 6% of the observed rate of change. The respiration term

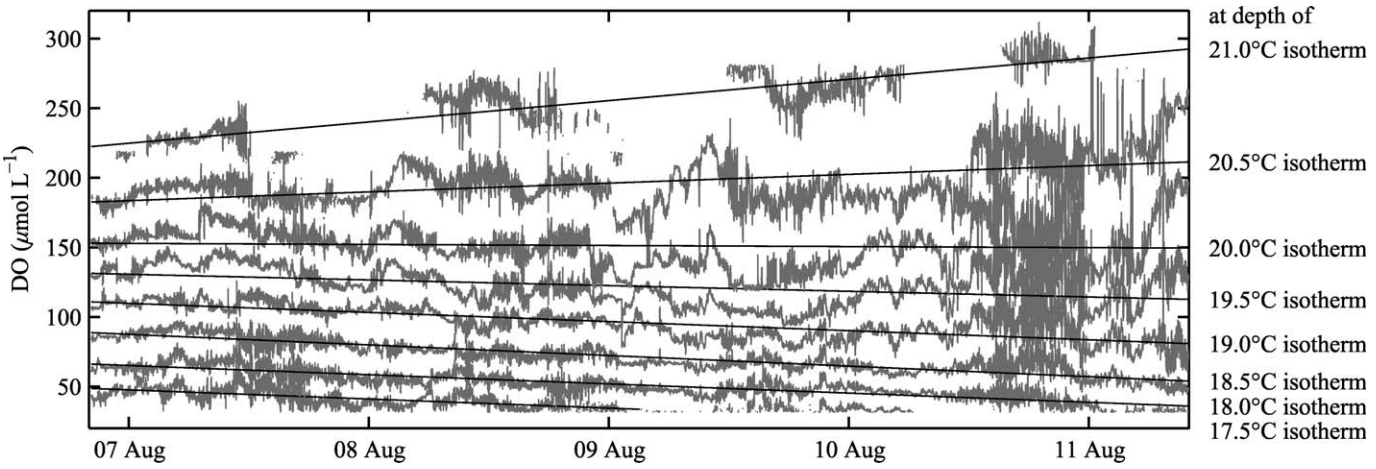

Fig. 8. DO concentrations at the depth of the isotherms denoted right of the panel (gray lines) with linear regressions (black lines). Regression coefficients of DO concentration vs. time at the 17.5–21°C isotherms (0.5°C increment) are −6.61, −6.57, −7.59, −6.58, −4.11, −0.75, 6.29, and 15.34 μmol L^{-1} d^{-1}. Data gaps result from isoline displacements beyond the measurement range of the moorings.

R_{net} in Eq. 4 must therefore account for the residual of the observed rate of change of DO concentration, and balancing both sides of Eq. 4 yields $R_{net} \approx -6.2$ μmol L^{-1} d^{-1}. The relatively constant decrease of DO concentration at isothermal depth (Fig. 8) indicates that the oxygen consumption rate is nearly constant within the oxycline.

During our measurements, the lower and upper bound of the oxycline corresponded roughly to the locations of the 17.5°C and 19°C isotherm, respectively (Fig. 8), resulting in a vertical extent of the oxycline that varied between 0.5 and 3.3 m with a mean value of 1.5 m (h_{oxy}). Applying the estimated R_{net} to this layer results in a total (depth-integrated) DO consumption rate of −9.3 mmol m^{-2} d^{-1}, which is in close agreement with the mean EC flux measured above the oxycline (−15.9 mmol m^{-2} d^{-1} excluding the flux event). The highly variable flux measured by EC is thus balanced by a relatively constant DO uptake within the oxycline (Fig. 8). The observed strong temporal variation in DO fluxes does not appear to affect DO uptake in the oxycline on the same temporal scale, since DO uptake is rather constant with time (Fig. 8). Therefore, temporal variation in DO fluxes rather affects the storage of DO in the upper part of the oxycline, where diffusivities are episodically enhanced by turbulence (e.g., 21°C isotherm in Fig. 8).

DO sources and sinks—Major processes contributing to the total rate of DO consumption within the oxycline are primary production (PP), biological respiration and mineralization (R_{biol}), and chemical oxygen consumption due to the oxidation of reduced substances (R_{chem}; Fig. 9). Measurements of depth profiles of photosynthetically active radiation (PAR) conducted twice during our measurements (data not shown) revealed a compensation depth (defined as the depth where PAR is attenuated to 1% of its value at the water surface) of about 7 m, indicating that there was little to no net primary production occurring within the oxycline.

The observed mean total DO equivalent flux from the hypolimnion into the oxycline derived from fluxes of reduced substances (−0.14 mmol m^{-2} d^{-1} excluding S^{2-}, −0.19 mmol m^{-2} d^{-1} including S^{2-}) accounts for 29–38% of the total mean DO flux at the lower end of the oxycline (−0.49 mmol m^{-2} d^{-1}). Considering this hypolimnetic chemical oxygen consumption as an upper limit of R_{chem} in the oxycline, it is still 50 times smaller than the part of total DO consumption in the oxycline ascribed to R_{net} of −9.3 mmol m^{-2} d^{-1}, indicating that the oxidation of reduced substances transported upward from the anoxic hypolimnion constitutes a minor component of R_{net}.

In summary, biological respiration and mineralization R_{biol} can be considered as the main process determining R_{net} in the oxycline, accounting for 92% of the temporal change in the oxycline. This oxygen demand is associated with microbial mineralization of organic matter and must be balanced by a corresponding primary production and export from the overlaying epilimnion, as well as by an upward flux of mineralized (inorganic) carbon and nutrients. The seasonal mean net epilimnetic primary production in Lake Scharmützelsee was reported in 1996 to be 280 mmol m^{-2} d^{-1} (Schmitt and Nixdorf 1998). Recent production rates are probably much lower because the lake has been recovering from eutrophication in the past decade (Grüneberg et al. 2011), and the order of magnitude suggests that the estimated mineralization rate within the oxycline can be supported by the export of organic carbon from the epilimnion.

The observed DO flux into the oxycline must be balanced by gas exchange at the lake surface or by primary production in the epilimnion. Atmospheric DO fluxes during our sampling period were estimated following Wanninkhof (1992) with piston velocities calculated according to Crusius and Wanninkhof (2003) and ranged from −73.1 to 11.2 mmol m^{-2} d^{-1} with an average of −5.6 ± 27.8 mmol m^{-2} d^{-1} (Fig. 9). This value is in the same order of magnitude as the DO flux into the oxycline, suggesting that during our sampling period, primary production in the epilimnion was contributing to DO transport into the oxycline at most within the same order of magnitude.

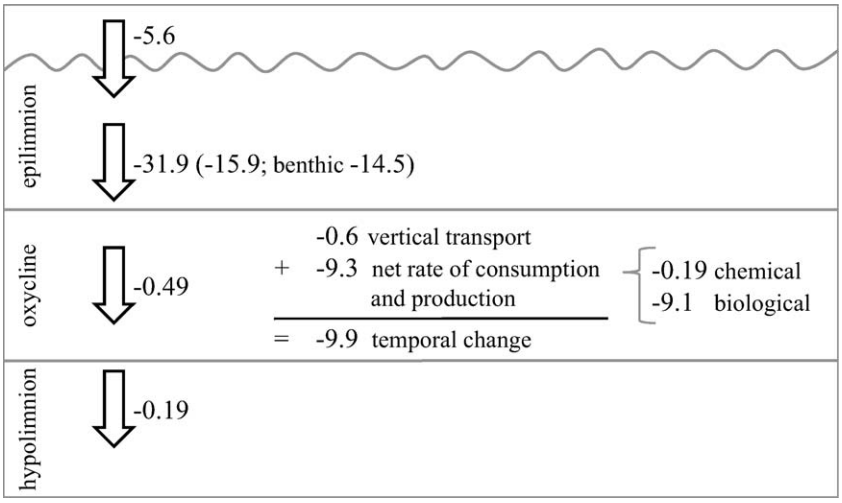

Fig. 9. Summary of all fluxes in the epilimnion and within and across the oxycline in mmol DO m^{-2} d^{-1}. The DO flux in the hypolimnion represents the DO equivalent of upward transported reduced substances. The downward flux above the oxycline is supplemented by the DO flux excluding the flux event (in parentheses). Rates were transformed to fluxes by multiplication with mean oxycline thickness h_{oxy}. Temporal change of DO concentration within the oxycline ($\partial C/\partial t$) is composed of vertical transport (mixing) and the net rate of oxygen consumption and production (R_{net}). The latter summarizes primary production, biological respiration and mineralization (R_{biol}), and chemical oxygen consumption (R_{chem}), where R_{biol} is the only term that is not based on conducted measurements.

Significance of pelagic oxyclines for biogeochemical cycling—Our estimate of the mean volume-specific DO consumption rate within the oxycline (R_{net}) is in close correspondence with the hypolimnetic oxygen depletion rate of -5.94 μmol L^{-1} d^{-1} estimated by Nixdorf et al. (1995) for Lake Scharmützelsee and is in the same order of magnitude as hypolimnetic oxygen depletion rates of other eutrophic lakes (Müller et al. 2012; Bouffard et al. 2013). Müller et al. (2012) analyzed data from 11 lakes and derived a model describing the consumption of DO in the hypolimnia of eutrophic lakes as a result of only two fundamental processes: DO consumption at the sediment surface due to mineralization of settled biomass and upward diffusion of reduced substances. Interestingly, the total oxygen consumption estimated for the oxycline in the present study is in close agreement with the intrinsic DO consumption rate estimated by Müller et al. (2012) for lakes having no or only a very thin hypolimnion, i.e., in the range of the thickness of the oxycline of 1.5 m. However, in contrast to the assumptions made in the model of Müller et al. (2012), our measurements show that most of the mineralization occurs within the oxycline and not in the sediment, while the upward flux of reduced substances provides only a small contribution to the total DO uptake. This difference can be attributed to the presence of an anoxic hypolimnion and the prevalence of only weak vertical transport rates within the oxycline observed in the present study. The former results in the temporal decoupling of the accumulation of biomass and reduced substances in the hypolimnion during summer stratification and its final oxidation during lake overturn. The latter restricts DO transport to the hypolimnion compared with the settling of organic particles, leading to an imbalance in the export of DO and carbon and thereby facilitating the decoupling. Our findings indicate that under such conditions, DO consumption and therewith mineralization within the oxycline can be of comparable magnitude as the corresponding rates occurring in the sediments of eutrophic lakes with an oxic hypolimnion. This result is further supported by the observations that DO fluxes above pelagic and benthic oxyclines are of comparable magnitude. The latter finding differs from the observations of Bouffard et al. (2013) in Lake Erie, where the mean DO flux across the thermocline was one order of magnitude smaller than the flux across the sediment–water interface. A regime shift from a dominance of benthic to pelagic mineralization can be expected to result in short-circuiting of lake-internal nutrient and carbon fluxes and an increase of corresponding turnover rates. Turbulent mixing, which is the major factor controlling vertical fluxes, is strongly affected by density stratification, and situations where turbulence is suppressed can be expected to occur more frequently in aquatic systems under current climate change scenarios (Livingstone 2003; Peeters et al. 2007). The increase of nutrient and carbon turnover rates caused by the formation of pelagic oxyclines might therefore provide an important, but yet unexplored, response of aquatic ecosystems to climatic changes.

Acknowledgments

We thank S. Geissler, E. Sünger, and M. Wieprecht for their help in the field. Thanks to B. Grüneberg and J. Rücker (Brandenburg University of Technology Cottbus-Senftenberg) for providing weather data and lake bathymetry, A. Kleeberg (Leibniz-Institute of Freshwater Ecology and Inland Fisheries) for

contributing data on sulfide concentrations, and A. Glud (University of Southern Denmark) for providing the microelectrodes used in this study. S. MacIntyre and E. Tedford made available the software used for analyzing the microstructure profiles. C. Bluteau shared Matlab scripts for maximum-likelihood inertial subrange fitting. The Water Analytics team and the Workshop team of the Helmholtz Centre for Environmental Research are acknowledged for analytical and technical support. We thank two anonymous reviewers for their comments, which substantially improved the manuscript. This study was financially supported by the German Research Foundation (DFG), grants LO 1150/4-1 and KO 1911/5-1.

References

Adrian, R., R. Deneke, U. Mischke, R. Stellmacher, and P. Lederer. 1995. Long-term study of the Heiligensee (1975–1992)—evidence for effects of climatic-change on the dynamics of eutrophied lake ecosystems. Arch. Hydrobiol. **133:** 315–337.

Baker, M. A., and C. H. Gibson. 1987. Sampling turbulence in the stratified ocean: Statistical consequences of strong intermittency. J. Phys. Oceanogr. **17:** 1817–1836, doi:10.1175/1520-0485(1987)017<1817:STITSO>2.0.CO;2

Bluteau, C. E., N. L. Jones, and G. N. Ivey. 2011. Estimating turbulent kinetic energy dissipation using the inertial subrange method in environmental flows. Limnol. Oceanogr. Methods **9:** 302–321, doi:10.4319/lom.2011.9.302

Boehrer, B., and M. Schultze. 2008. Stratification of lakes. Rev. Geophys. **46:** RG2005, doi:10.1029/2006RG000210

Bouffard, D., J. D. Ackerman, and L. Boegman. 2013. Factors affecting the development and dynamics of hypoxia in a large shallow stratified lake: Hourly to seasonal patterns. Water Resour. Res. **49:** 2380–2394, doi:10.1002/wrcr.20241

———, and L. Boegman. 2013. A diapycnal diffusivity model for stratified environmental flows. Dyn. Atmos. Oceans **61–62:** 14–34, doi:10.1016/j.dynatmoce.2013.02.002

Brand, A., D. F. McGinnis, B. Wehrli, and A. Wüest. 2008. Intermittent oxygen flux from the interior into the bottom boundary of lakes as observed by eddy correlation. Limnol. Oceanogr. **53:** 1997–2006, doi:10.4319/lo.2008.53.5.1997

Bryant, L. D., C. Lorrai, D. F. McGinnis, A. Brand, A. Wüest, and J. C. Little. 2010. Variable sediment oxygen uptake in response to dynamic forcing. Limnol. Oceanogr. **55:** 950–964, doi:10.4319/lo.2009.55.2.0950

Chen, C.-T., and F. J. Millero. 1977. The use and misuse of pure water PVT properties for lake waters. Nature **266:** 707–708, doi:10.1038/266707a0

Crusius, J., and R. Wanninkhof. 2003. Gas transfer velocities measured at low wind speed over a lake. Limnol. Oceanogr. **48:** 1010–1017, doi:10.4319/lo.2003.48.3.1010

Davis, R. E. 1996. Sampling turbulent dissipation. J. Phys. Oceanogr. **26:** 341–358, doi:10.1175/1520-0485(1996)026<0341:STD>2.0.CO;2

Davison, W. 1981. Supply of iron and manganese to an anoxic lake basin. Nature **290:** 241–243, doi:10.1038/290241a0

Dunckley, J. F., J. R. Koseff, J. V. Steinbuck, S. G. Monismith, and A. Genin. 2012. Comparison of mixing efficiency and vertical diffusivity models from temperature microstructure. J. Geophys. Res. **117:** C10008, doi:10.1029/2012JC007967

Emery, W. J., and R. E. Thomson. 1997. Data analysis methods in physical oceanography, 2nd rev. ed. Elsevier.

Foley, B., I. D. Jones, S. C. Maberly, and B. Rippey. 2012. Long-term changes in oxygen depletion in a small temperate lake: Effects of climate change and eutrophication. Freshw. Biol. **57:** 278–289, doi:10.1111/j.1365-2427.2011.02662.x

Gargett, A. E., T. R. Osborn, and P. W. Nasmyth. 1984. Local isotropy and the decay of turbulence in a stratified fluid. J. Fluid Mech. **144:** 231–280, doi:10.1017/S0022112084001592

Goldenfum, J. A. [ed.]. 2010. GHG measurement guidelines for freshwater reservoirs. The International Hydropower Association (IHA).

Goring, D., and V. Nikora. 2002. Despiking acoustic doppler velocimeter data. J. Hydraul. Eng. **128:** 117–126, doi:10.1061/(ASCE)0733-9429(2002)128:1(117)

Goudsmit, G. H., F. Peeters, M. Gloor, and A. Wüest. 1997. Boundary versus internal diapycnal mixing in stratified natural waters. J. Geophys. Res. Oceans **102:** 27903–27914, doi:10.1029/97JC01861

Grüneberg, B., J. Rücker, B. Nixdorf, and H. Behrendt. 2011. Dilemma of non-steady state in lakes—development and predictability of in-lake P concentration in dimictic lake Scharmützelsee (Germany) after abrupt load reduction. Int. Rev. Hydrobiol. **96:** 599–621, doi:10.1002/iroh.201111287

Imberger, J. 1998. Flux paths in a stratified lake: A review, p. 1–18. *In* J. Imberger [ed.], Physical processes in lakes and oceans. Coastal and estuarine studies. American Geophysical Union.

Imboden, D. M., and A. Wüest. 1995. Mixing mechanisms in lakes, p. 83–138. *In* A. Lerman, D. Imboden, and J. Gat [eds.], Physics and chemistry of lakes. Springer.

Ivey, G. N., K. B. Winters, and J. R. Koseff. 2008. Density stratification, turbulence, but how much mixing? Annu. Rev. Fluid Mech. **40:** 169–184, doi:10.1146/annurev.fluid.39.050905.110314

Kleeberg, A. 1997. Interactions between benthic phosphorus release and sulfur cycling in lake Scharmützelsee (Germany). Water, Air, Soil Pollut. **99:** 391–399.

Kocsis, O., H. Prandke, A. Stips, A. Simon, and A. Wuest. 1999. Comparison of dissipation of turbulent kinetic energy determined from shear and temperature microstructure. J. Mar. Syst. **21:** 67–84, doi:10.1016/S0924-7963(99)00006-8

Livingstone, D. M. 2003. Impact of secular climate change on the thermal structure of a large temperate central European lake. Clim. Change **57:** 205–225, doi:10.1023/A:1022119503144

Lorke, A. 2007. Boundary mixing in the thermocline of a large lake. J. Geophys. Res. **112:** C09019, doi:10.1029/2006JC004008

———, D. F. McGinnis, and A. Maeck. 2013. Eddy-correlation measurements of benthic fluxes under complex flow conditions: Effects of coordinate transformations and averaging time scales. Limnol. Oceanogr. Methods **11:** 425–437, doi:10.4319/lom.2013.11.425

———, B. Müller, M. Maerki, and A. Wüest. 2003. Breathing sediments: The control of diffusive transport across the sediment-water interface by periodic boundary-layer turbulence. Limnol. Oceanogr. **48:** 2077–2085, doi:10.4319/lo.2003.48.6.2077

———, and A. Wüest. 2005. Application of coherent ADCP for turbulence measurements in the bottom boundary layer. J. Atmos. Oceanic Technol. **22:** 1821–1828, doi:10.1175/JTECH1813.1

Lorrai, C., D. F. McGinnis, P. Berg, A. Brand, and A. Wüest. 2010. Application of oxygen eddy correlation in aquatic systems. J. Atmos. Oceanic Technol. **27:** 1533–1546, doi:10.1175/2010JTECHO723.1

MacIntyre, S., K. M. Flynn, R. Jellison, and J. Romero. 1999. Boundary mixing and nutrient fluxes in Mono Lake, California. Limnol. Oceanogr. **44:** 512–529, doi:10.4319/lo.1999.44.3.0512

Matzinger, A., B. Müller, P. Niederhauser, M. Schmid, and A. Wüest. 2010. Hypolimnetic oxygen consumption by sediment-based reduced substances in former eutrophic lakes. Limnol. Oceanogr. **55:** 2073–2084, doi:10.4319/lo.2010.55.5.2073

McGinnis, D. F., P. Berg, A. Brand, C. Lorrai, T. J. Edmonds, and A. Wüest. 2008. Measurements of eddy correlation oxygen fluxes in shallow freshwaters: Towards routine applications and analysis. Geophys. Res. Lett. **35:** L04403, doi:10.1029/2007GL032747

———, S. Cherednichenko, S. Sommer, P. Berg, L. Rovelli, R. Schwarz, R. N. Glud, and P. Linke. 2011. Simple, robust eddy correlation amplifier for aquatic dissolved oxygen and hydrogen sulfide flux measurements. Limnol. Oceanogr. Methods **9:** 340–347, doi:10.4319/lom.2011.9.340

Miles, J. W. 1961. On the stability of heterogeneous shear flows. J. Fluid Mech. **10:** 496–508, doi:10.1017/S0022112061000305

Moncrieff, J., R. Clement, J. Finnigan, and T. Meyers. 2010. Averaging, detrending, and filtering of eddy covariance time series, p. 7–31. *In* X. Lee, W. Massman, and B. Law [eds.], Handbook of micrometeorology—a guide for surface flux measurement and analysis. Atmospheric and Oceanographic Sciences Library. Kluwer.

Müller, B., L. D. Bryant, A. Matzinger, and A. Wüest. 2012. Hypolimnetic oxygen depletion in eutrophic lakes. Environ. Sci. Technol. **46:** 9964–9971.

Nixdorf, B., J. Rücker, R. Deneke, and P. Zippel. 1995. Limnologische Zustandsanalyse von Standgewässern im Scharmützelseegebiet Teil 1. BTU Cottbus, Fakultät Umweltwissenschaften und Verfahrenstechnik, Eigenverlag. [Limnological analysis of the condition of water bodies in the Scharmützelsee region Part 1.]

Peeters, F., D. Straile, A. Lorke, and D. M. Livingstone. 2007. Earlier onset of the spring phytoplankton bloom in lakes of the temperate zone in a warmer climate. Glob. Change Biol. **13:** 1898–1909, doi:10.1111/j.1365-2486.2007.01412.x

Revsbech, N. P. 1989. An oxygen microsensor with a guard cathode. Limnol. Oceanogr. **34:** 474–478, doi:10.4319/lo.1989.34.2.0474

Rodrigo, M. A., M. R. Miracle, and E. Vicente. 2001. The meromictic Lake La Cruz (Central Spain). Patterns of stratification. Aquat. Sci. **63:** 406–416, doi:10.1007/s00027-001-8041-x

Ruddick, B., A. Anis, and K. L. Thompson. 2000. Maximum likelihood spectral fitting: The batchelor spectrum. J. Atmos. Oceanic Technol. **17:** 1541–1555, doi:10.1175/1520-0426(2000)017<1541:MLSFTB>2.0.CO;2

Schmitt, M., and B. Nixdorf. 1998. Gewässerreport (Nr. 4): Forschungsergebnisse zur Limnologie von Gewässern im Scharmützelseegebiet und in Bergbaufolgelandschaften. BTUC-AR 5/98. [Research findings on the limnology of water bodies in the Scharmützelsee region and former mining landscapes.]

Shih, L. H., J. R. Koseff, G. N. Ivey, and J. H. Ferziger. 2005. Parameterization of turbulent fluxes and scales using homogeneous sheared stably stratified turbulence simulations. J. Fluid Mech. **525:** 193–214, doi:10.1017/S0022112004002587

Steinbuck, J. V., M. T. Stacey, and S. G. Monismith. 2009. An evaluation of χT estimation techniques: Implications for batchelor fitting and ε. J. Atmos. Oceanic Technol. **26:** 1652–1662, doi:10.1175/2009JTECHO611.1

Turner, L., and W. D. Erskine. 2005. Variability in the development, persistence and breakdown of thermal, oxygen and salt stratification on regulated rivers of southeastern Australia. River Res. Appl. **21:** 151–168, doi:10.1002/rra.838

Wanninkhof, R. 1992. Relationship between wind-speed and gas-exchange over the ocean. J. Geophys. Res.—Oceans **97:** 7373–7382, doi:10.1029/92JC00188

Wetzel, R. G. 2001. Limnology, 3rd ed. Academic.

Wüest, A., and A. Lorke. 2003. Small-scale hydrodynamics in lakes. Annu. Rev. Fluid Mech. **35:** 373–412, doi:10.1146/annurev.fluid.35.101101.161220

Zhang, H. Y., S. A. Ludsin, D. M. Mason, A. T. Adamack, S. B. Brandt, X. S. Zhang, D. G. Kimmel, M. R. Roman, and W. C. Boicourt. 2009. Hypoxia-driven changes in the behavior and spatial distribution of pelagic fish and mesozooplankton in the northern Gulf of Mexico. J. Exp. Mar. Biol. Ecol. **381:** 80–91, doi:10.1016/j.jembe.2009.07.014

Associate editor: John M. Melack

Received: 15 November 2013
Accepted: 19 June 2014
Amended: 08 June 2014